



Dynamics of dissociative electron attachment to ammonia

T. N. Rescigno,¹ C. S. Trevisan,² A. E. Orel,³ D. S. Slaughter,¹ H. Adaniya,¹ A. Belkacem,¹ Marvin Weyland,^{4,5} Alexander Dorn,⁵ and C. W. McCurdy^{1,6}

¹Lawrence Berkeley National Laboratory, Chemical Sciences, Berkeley, California 94720, USA

²Department of Sciences and Mathematics, California Maritime Academy, Vallejo, California 94590, USA

³Department of Chemical Engineering and Materials Science, University of California, Davis, California 95616, USA

⁴Physikalisch-Technische Bundesanstalt, 38116 Braunschweig, Germany

⁵Max-Planck-Institut für Kernphysik, 69117 Heidelberg, Germany

⁶Department of Chemistry, University of California, Davis, California 95616, USA

(Received 1 March 2016; published 12 May 2016)

Ab initio theoretical studies and momentum-imaging experiments are combined to provide a consistent picture of the dynamics of dissociative electron attachment to ammonia through its 5.5- and 10.5-eV resonance channels. The present study clarifies the character and symmetry of the anion states involved and the dynamics that leads to the observed fragment-ion channels, their branching ratios, and angular distributions.

DOI: [10.1103/PhysRevA.93.052704](https://doi.org/10.1103/PhysRevA.93.052704)

I. INTRODUCTION

Low-energy electron collisions with small molecules are often characterized by the formation of transient negative ions. The cross sections for formation of these anions can be large and often lead to dissociation into reactive negative-ion and neutral fragments. The dynamics associated with these dissociative processes can be complex, involving conical intersections between different anion states and multiple fragment-ion product channels [1–4]. The laboratory-frame angular distributions of fragment ions can provide a unique insight into understanding the breakup process since they often contain signatures of the symmetry of the resonance state and are a key ingredient in unraveling the underlying dynamics of dissociative electron attachment (DEA) [4–6]. In favorable cases where the dissociation is prompt, we have shown that the theoretically obtained electron entrance amplitude, which ties the molecular to the laboratory frame, can be used to predict laboratory-frame angular distributions and identify specific dissociation mechanisms. These distributions can be compared with experimental measurements to confirm the predictions.

The ammonia molecule offers an interesting case in point. A number of early experimental studies established that there are two principal channels for DEA to NH_3 , centered around 5.5 and 10.5 eV [7–9]. The first channel produces both H^- and NH_2^- , in a ratio of $\sim 6 : 4$ [10], while the higher-energy channel produces predominantly H^- , small amounts of NH_2^- and even smaller amounts of NH^- . The $\text{NH}_2^- (^1A_1) + \text{H} (^2S)$ and $\text{NH}_2 (^2B_1) + \text{H} (^1S)$ dissociation channels have similar thermodynamic thresholds, the $\text{NH}_2^- + \text{H}$ asymptote lying only ~ 0.02 eV below the $\text{NH}_2 + \text{H}^-$ asymptote [11]. Moreover, since both channels are nondegenerate, they cannot be correlated to the same anion state. Yet, both product channels are produced from the same 5.5-eV resonance band. Another curious feature of the 5.5-eV DEA resonance is the series of overlapping peaks in the total cross sections for both H^- and NH_2^- production, first observed by Stricklett and Burrow [12]. These have been attributed to umbrella-mode oscillations in the negative ion, similar to those observed in the optical absorption [13] and photoelectron [14] spectra of neutral NH_3 . In a recent study, Ram and Krishnakumar [15] have measured H^- and

NH_2^- fragment ions from both the 5.5- and 10.5-eV DEA resonances using the velocity-slice imaging [16] technique and obtained angular and ion kinetic-energy distributions for both species.

In contrast to the comprehensive body of experimental data on ammonia DEA, there has been little theoretical work on this system. There have been a handful of theoretical calculations on elastic electron- NH_3 scattering dating back to the early 1990s [17–19], but no previous theoretical studies of DEA or negative-ion NH_3^- states. The scattering calculations indicate the presence of a very broad *d*-wave shape resonance peaking near 10 eV, but it is not clear what role, if any, it plays in the DEA dynamics. We have therefore undertaken the present study, using electronic structure calculations, fixed-nuclei electron scattering calculations, and time-dependent wavepacket dynamics to fully characterize the principal features of DEA dynamics in this system. We have also undertaken independent momentum-imaging [20,21] measurements at two different laboratories whose results are interpreted with the aid of our theoretical calculations to arrive at an understanding of the negative-ion resonances and the dynamics that lead to the observed DEA angular distributions.

II. THEORETICAL FORMULATION

A. Fixed-nuclei scattering and computation of entrance amplitudes

In its electronic ground state, ammonia has C_{3v} symmetry and is nominally described by the single configuration wave function $1a_1^2 2a_1^2 1e^4 3a_1^2$, 1A_1 . Given the absence of any narrow negative-ion shape resonances, it follows that DEA in ammonia proceeds through Feshbach resonances which are formed in electron collisions which excite an occupied valence electron ($3a_1$ or $1e$) and capture two electrons into the lowest unoccupied $4a_1$ orbital (LUMO), the latter having mixed valence-Rydberg ($3s$) character. By analogy to what we find in the case of DEA to water [22], the NH_3^- negative-ion resonances have the configurations $1a_1^2 2a_1^2 1e^4 3a_1 4a_1^2$, 2A_1 and $1a_1^2 2a_1^2 1e^3 3a_1^2 4a_1^2$, 2E , the latter being doubly degenerate. This expectation was born out in complex Kohn scattering

calculations [23], carried out in neutral equilibrium geometry, which form the basis of our theoretical treatment of DEA [5].

We start with a self-consistent-field (SCF) calculation on neutral ammonia, followed by an improved virtual orbital (IVO) calculation [24] to obtain the $4a_1$ LUMO. The calculations were carried out with Dunning's triple- η basis [25], augmented with additional (two s -type, two p -type, and two d -type) diffuse functions on the nitrogen. This was followed by a multireference complete active space (CAS) singles and doubles configuration-interaction (CI) calculation to obtain the excited 3A_1 and 3E neutral states, which are the parents of the Feshbach resonances. The orbitals for the CAS space included the SCF occupied orbitals plus the $4a_1$ and $2e$ IVO orbitals. The eight natural orbitals with the largest occupation numbers for the 3A_1 and 3E states were used to construct the target states for the scattering calculations, the former for the lower resonance, the latter for the upper resonance. We found that a number of Rydberg neutral states appear between the first and second parent triplet states, so we carried out nine-channel scattering calculations that included all singlet and triplet target states up to and including the 3E parent resonance states in the close-coupling expansion.

The orbital basis used in these scattering calculations cannot represent all of the Rydberg states below the upper resonance. In separate calculations in a larger basis we found three 3E and three 3A_1 states lying below the parent triplet 3E ($1e \rightarrow 4a_1$) state of the upper resonance. The spectroscopic experimental observation of the associated singlets [26] reveals that at least the same number of singlet Rydberg states (and probably more) lie below the parent state of the upper resonance at the equilibrium geometry with C_{3v} symmetry. Since these Rydberg states are not the parents of other observed resonances and are weakly coupled to the $1,{}^3E$ parent configurations of the upper resonance, their exclusion as channels from the present Kohn variational scattering calculations is not expected to significantly alter the results.

The positions, E_R , and widths, Γ , of the two Feshbach resonances were obtained by fitting the eigenphase sums from the fixed-nuclei scattering calculations at equilibrium geometry to a Breit-Wigner form, giving $E_R = 4.19$ eV, $\Gamma = 0.011$ eV for the lower resonance and $E_R = 10.36$ eV, $\Gamma = 0.033$ eV for the upper resonance. Note that the positions, E_R , are with respect to the NH_3 ground state and are somewhat smaller than observed, because the molecular orbitals used in the calculations were optimized for the parent excited states. It is also important to bear in mind that the measured DEA peaks have widths of several eV. The observed width is not determined by the intrinsic fixed-nuclei electronic width of the resonance but rather by the variation of the dissociative resonance energy surface relative to the neutral target state over the Franck-Condon region.

To connect the theoretical results, which are computed in the molecular frame, to laboratory-frame angular distributions, we calculate the entrance amplitude, as described at length in Refs. [4] and [5]. The entrance amplitude is a complex quantity defined as a matrix element of the electronic Hamiltonian between the resonance wave function Ψ_{res} and a background scattering wave function Ψ_{bg} , the latter characterized by an electron with momentum vector \mathbf{k} , defined by polar angles θ

and ϕ , incident on a fixed-in-space molecule,

$$\begin{aligned} V(\theta, \phi; \Xi) &= \langle \Psi_{\text{res}}(\Xi) | H_{\text{el}} | \Psi_{\text{bg}}(\theta, \phi; \Xi) \rangle \\ &\equiv \langle Q\Psi | H_{\text{el}} | P\Psi \rangle, \end{aligned} \quad (1)$$

where Ξ labels the internal coordinates of the molecule and the integration implied is over the electronic coordinates. Direct calculation of the PQ matrix element is complicated by the fact that the background wave function must be computed with a Hamiltonian from which the resonance has been projected. Alternatively, the entrance amplitude can also be defined in terms of the residue of the fixed-nuclei S matrix at the complex resonance energy.

We make use of the form of the S matrix near a narrow resonance, as outlined in Ref. [5], and write S as [27]

$$S = S^{bg\ 1/2}(E) \left(1 - \frac{iA}{E - E_r + i\Gamma/2} \right) S^{bg\ 1/2}(E), \quad (2)$$

where S^{bg} is the slowly varying background part of the S matrix and A is a rank 1 Hermitian matrix. In a partial-wave representation, we can thus write

$$A_{lm, l'm'}^{\Lambda\Lambda'} = \delta_{lm}^{\Lambda} \delta_{l'm'}^{*\Lambda'}, \quad (3)$$

where Λ labels an electronically open channel. Time-reversal invariance requires the S matrix to be symmetric. This, in turn, requires the δ_{lm}^{Λ} to be real, so the complex conjugation sign in Eq. (3) can be dropped.

We make use of the unitarity of S^{bg} to write

$$S^{bg}(E) = U\Omega(E)U^\dagger, \quad (4)$$

where U is the unitary transformation that diagonalizes S^{bg} and Ω is a diagonal matrix of eigenvalues, $\Omega_{\alpha, \beta}(E) = \delta_{\alpha\beta} e^{i2\phi_\alpha^{\text{bg}}(E)}$. We are using α as a collective index of the quantum numbers needed to specify a channel labeled by electronic target state and electron angular momentum indices (Λ, l, m) . With these definitions, we can express the S matrix as

$$S = S^{bg} + UBU^\dagger, \quad (5)$$

where the matrix elements of B are given by

$$\begin{aligned} B_{lm, l'm'}^{\Lambda\Lambda'} &= -i \left(\frac{e^{i\phi_0^{\Lambda lm}} \delta_{lm}^{\Lambda} e^{i\phi_0^{\Lambda' l'm'}} \delta_{l'm'}^{\Lambda'}}{E - E_r + i\Gamma/2} \right) \\ &\equiv i \left(\frac{\gamma_{lm}^{\Lambda} \gamma_{l'm'}^{\Lambda'}}{E - E_r + i\Gamma/2} \right). \end{aligned} \quad (6)$$

The background eigenphases have been incorporated into γ_{lm}^{Λ} , which is a *complex* partial width describing decay of the resonance into the (Λ, l, m) background channel. Note that because of the energy dependence of the background eigenphases ϕ_0 , the partial widths are, in principle, energy dependent. However, because the magnitude of B is strongly peaked in the energy range $E_R - \Gamma/2 < E < E_R + \Gamma/2$ and Γ is small by assumption, we can assume the partial widths to be constant, i.e., that $\gamma_{lm}^{\Lambda}(E) \approx \gamma_{lm}^{\Lambda}(E_R)$. Unitarity of S then demands that [28]

$$\Gamma = \sum_{\Gamma, l, m} |\gamma_{lm}^{\Lambda}|^2. \quad (7)$$

In fitting our computed S -matrix elements to the expressions given by Eqs. (5) and (6), we found that the background S

matrix was well fit with a quadratic polynomial in E . The overall accuracy of the fit was established by checking that Eq. (7) was well satisfied.

When the relative orientation of the fragments is not observed, as is generally the case, the angular distribution of the DEA product ions is given by

$$\begin{aligned} \frac{d\sigma_{\text{DEA}}}{d\theta} &\propto \int d\phi |V(\theta, \phi; \Xi)|^2 \\ &= \int d\phi \left| \sum_{l,m} i^l \gamma_{lm}^{\Lambda_0} Y_{lm}^*(\theta, \phi) \right|^2, \end{aligned} \quad (8)$$

where the sum is only over the partial widths associated with the incident electronic channel Λ_0 . We take the body-frame z axis to coincide with the recoil axis, so that θ and ϕ represent the orientation of the incident electron relative to the dissociation axis in the molecular frame. If the laboratory-frame recoil axis is different from the body-frame z axis in which the scattering calculations are performed, we can rotate the partial widths before computing the entrance amplitude,

$$\gamma_{lm}^{\Lambda} \rightarrow \sum_{m'} D_{m'm}^J(\alpha, \beta, \gamma) \gamma_{lm'}^{\Lambda}, \quad (9)$$

where $D_{m'm}^J$ is a Wigner rotation matrix element and α, β, γ are the Euler angles which orient the molecule in the new coordinate system. Rotation of the entrance probability can also be used to simulate the effect of nonaxial recoil, as we see below.

B. Computation of resonance potential-energy curves

To further characterize the resonance states away from C_{3v} geometry, we carried out multireference configuration-interaction (MRCI) calculations, using the Columbus program [29]. For these calculations, we used Dunning's aug-cc-pvtz

basis [30], deleting f -type functions on the nitrogen and d -type functions on the hydrogens, resulting in a basis of 71 contracted spherical Gaussian functions. To generate a set of molecular orbitals for the MRCI calculation, we obtained the natural orbitals from a singles-CI (CIS) calculation on the lowest triplet state of neutral NH_3 using ground-state SCF orbitals. For the calculations on the anion states, we carried out a multireference (complete active space or CAS) CIS, restricting the nitrogen $1s$ orbital to double occupancy and choosing an active space of seven orbitals and 63 virtual orbitals. There were $\sim 34\,000$ configurations in the CIS expansion and the lowest 25 roots were obtained.

The first set of calculations were done, starting in C_{3v} geometry, for various values of one N-H distance, holding the other two N-H distances and the H-N-H angles fixed. When one N-H bond is stretched, the symmetry of the system is lowered from C_{3v} to C_s with the reflection plane containing one hydrogen and the nitrogen atom, and the electronic states can only be labeled as A' or A'' . Note that these symmetry designations differ from those in earlier work [9,12], where the corresponding states are labeled in D_{3h} symmetry of a planar NH_3 molecular geometry. The lower resonance labeled here as 2A_1 (C_{3v}) or ${}^2A'$ (C_s) is designated ${}^2A''$ in those studies while the upper resonance here denoted 2E (C_{3v}) and its ${}^2A'$ (C_s) component are there designated as ${}^2A'_1$.

A second set of calculations was carried out to look at energy variations in the anion resonances under umbrella motion, i.e., as the angle between the NH bonds and the C_3 axis is varied about its equilibrium value of 68.2° . The anion potential curves for both N-H stretching and umbrella motion in C_{3v} symmetry are shown in Fig. 1.

At the equilibrium geometry, there are two roots whose largest contribution (CI coefficients ~ 0.9) come from the resonance configurations, $1e^4 3a_1 4a_1^2$ and $1e^3 3a_1^2 4a_1^2$, respectively. In tracking these resonances as the N-H distance

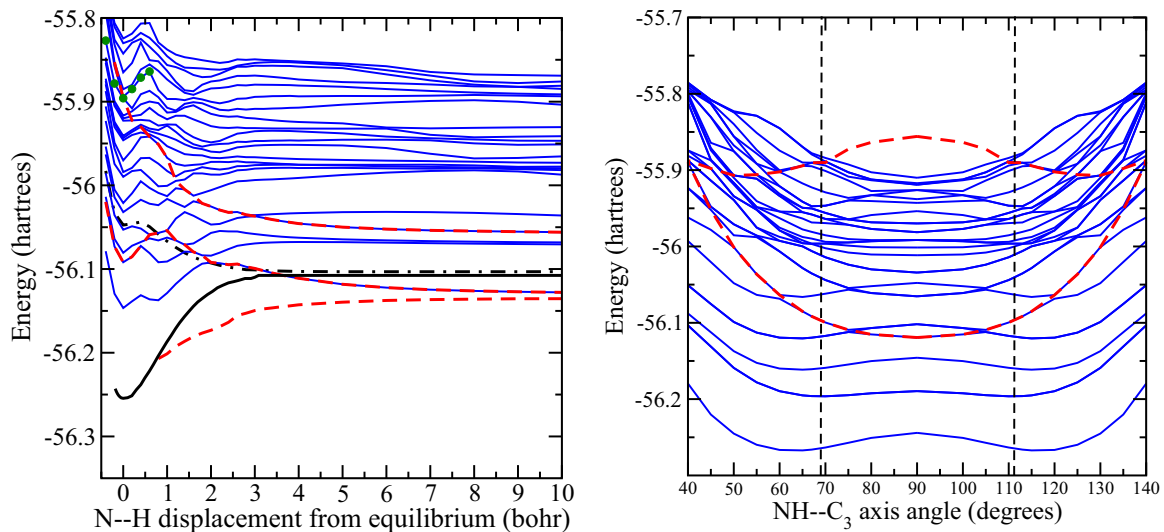


FIG. 1. NH_3^- potential-energy curves. (Left) HNH is fixed at equilibrium geometry as the third N-H distance is varied; the upper resonance (${}^2A''$), lower resonance (${}^2A'$), and virtual (${}^2A'$) states are shown as broken curves, while the solid lower curve and the dash-dotted curve are the ground and the lowest triplet state of the neutral molecule, respectively; the upper resonance, doubly degenerate at the equilibrium geometry of the neutral, splits into dissociative and nondissociative states away from equilibrium, the latter state indicated by solid circles. (Right) Umbrella motion with NH bond distances fixed at equilibrium value (1.9132 bohr); resonance states given as broken curves, vertical lines indicate equilibrium geometry of the neutral molecule.

is increased by ~ 2 bohr, numerous crossings with other discretized continuum states are encountered. By choosing the roots with the largest contribution coming from the resonance configurations, we arrive at the broken curves indicated in Fig. 1.

There are several points to note. The lower ${}^2A'$ resonance increases in energy by ~ 1 eV as the N-H distance is stretched by 1.0 bohr from equilibrium before decreasing monotonically to correlate with $H^- + NH_2$ (2B_1). This energy barrier is an indication that direct dissociation via axial recoil is unlikely for the lower resonance. Examination of the right panel of Fig. 1, however, shows that the 2A_1 resonance drops in energy by ~ 1.4 eV as the anion is flattened, an amount more than sufficient to overcome the initial barrier to dissociation. The upper resonance, which is doubly degenerate at equilibrium, splits into a dissociative ${}^2A'$ component, which correlates with $H^- + NH_2^*$ (2A_1), and a ${}^2A''$ component, which is not dissociative, as one N-H bond is stretched. The $NH_2^- + H$ asymptote correlates with neither resonance state, but rather decreases monotonically in energy as the N-H distance decreases and crosses the ground state of the neutral, becoming a virtual state, when the N-H displacement from equilibrium is ~ 1 bohr. This state is shown as the lowest broken curve in the left panel of Fig. 1.

A virtual state (or “antibound” state [31]) is not a localized state and there is no time delay associated with its formation [28]. While a virtual state may affect the threshold behavior of scattering cross sections, it does not offer a mechanism for electron capture as does a shape or a Feshbach resonance. In the present context, we must therefore conclude that population of the $NH_2^- + H$ channel cannot involve a direct process, but rather an indirect one where a resonance anion is first formed and the $NH_2^- + H$ channel subsequently populated through a charge-exchange process. To quantify this speculation, we carried out a third series of calculations at large N-H separations where the two lowest ${}^2A'$ anion channels are electronically bound and well separated from higher fragment channels. We started with a weighted, state-averaged multiconfiguration self-consistent-field (MCSCF) calculation on the two lowest triplet states of the neutral to obtain molecular orbitals for a singles and doubles CAS CI calculation on the two lowest anion states. The weights for the state-averaged MCSCF were adjusted at an N-H separation of 30 bohr so to give an energy separation of 0.02 eV between the anion states. We then computed the potential curves for the two states between 6.5 and 30 bohr with these weights (1.0 and 0.58). We also computed the nonadiabatic coupling elements between these states (see Sec. IV B.). The results are shown in Fig. 2. These results were used in time-dependent wave-packet calculations, which are described below.

We turn next to a description of the momentum-imaging experiments before presenting our results on DEA.

III. MOMENTUM-IMAGING EXPERIMENTS

The final momenta of anion fragments following DEA to ammonia were measured in two laboratories using the Lawrence Berkeley National Laboratory (LBNL) DEA reaction microscope and the Heidelberg reaction microscope. Each of the two reaction microscopes have been independently

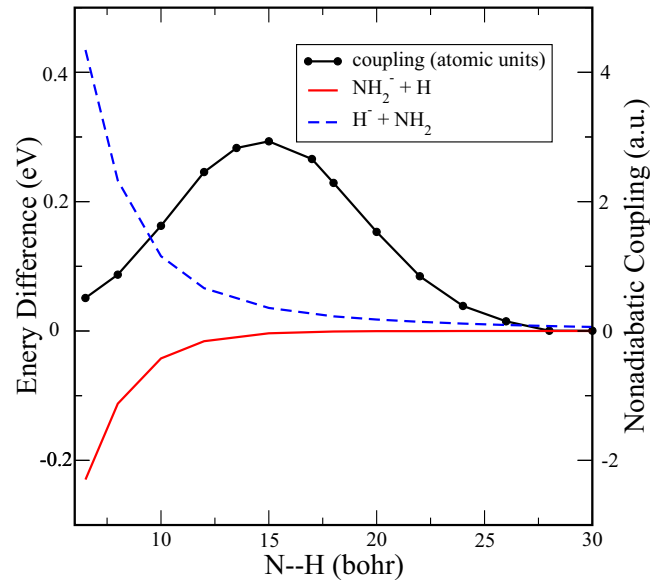


FIG. 2. Asymptotic NH_3^- potential-energy curves and nonadiabatic coupling, $|\langle h | \dot{h} \rangle|$. HNH is fixed at equilibrium geometry as the third N-H distance is varied.

developed and exhibit unique strengths and limitations. The important distinguishing characteristics relevant to the present study are that the Heidelberg reaction microscope has been recently developed to achieve very high resolution for heavier anion fragments. Due to high scattered electron background in the present experiments, H^- fragments could not be resolved from the background. On the other hand, the LBNL reaction microscope is capable of measuring all anion fragments, with relatively poor momentum resolution for the NH_2^- fragment, in the same experiment.

The LBNL experimental technique has been described in detail elsewhere [21], so only a brief outline is provided here. An effusive molecular beam of ammonia was formed using a stainless-steel capillary 20 mm in length and 0.3 mm in internal diameter to provide the target gas at the intersection of the electron beam. The electron beam consisted of 80-ns electron pulses at a 50-kHz repetition rate that were generated by a tunable electron gun and collimated with a ~ 25 -G axial magnetic field, which was formed by a pair of Helmholtz coils mounted externally to the vacuum chamber. The electron energy resolution was determined to be 0.8 eV, full width at half maximum, throughout these experiments. A pulsed repeller electrode, parallel and synchronized to the electron beam, extracted anions through a 25-mm grid to the shielded region of the spectrometer. The spectrometer shielding was necessary in addition to the magnetic field to avoid scattered electrons from being extracted along with anions into the spectrometer. Within the spectrometer anions with different masses were separated in their time of flight ($\sim 1.3 \mu s$ for H^-), while their momentum distribution resulted in corresponding distributions of their time of flight (typically ± 300 ns) and position at the anion detector. The anion detector was a three-dimensional position- and time-sensitive delay line anode of 80 mm nominal diameter. This experimental configuration allowed all anions to be detected in parallel with a 4π angular

acceptance. The raw detector coordinates were recorded in a list-mode format for off-line analysis, while a separate on-the-fly analysis was performed for real-time optimization of the experimental parameters. The system was periodically calibrated for momentum and electron energy offset against the well-known anion fragment momentum distributions for DEA to O₂ [21] and H₂O [22].

The Heidelberg reaction microscope performs the same type of measurements but differs from the LBNL apparatus in several key features, namely target gas delivery, electron gun, and spectrometer field geometry. For the target preparation, a supersonic jet is created by expanding the target gas through a 30- μ m nozzle and selecting the molecules with low transverse momentum by two skimmers, 250 and 400 μ m in diameter, a few millimeters and 2 cm downstream of the nozzle, respectively. The resulting supersonic jet has a low internal temperature, on the order of 10 K, which allows more accurate measurements of slow fragments. The pulsed electron beam is created using the photoemission gun described by Schröter *et al.* [32]. In short, the electron source consists of a Zn-doped GaAs crystal which is coated by a monolayer of cesium and oxygen to create a negative electron affinity. The electrons are emitted by illuminating the crystal with a pulsed laser beam at a wavelength of 786 nm and are focused and guided to the gas jet using einzel lenses and a magnetic field of 17 G along the electron beam direction. The spectrometer consists of three regions, the interaction region in which the electric field is switched on by applying a voltage pulse to the pusher plate, 1 μ s after the ions are created, the acceleration region and the drift region. In the combined interaction and acceleration region the ions are accelerated by a 70-V potential difference which is chosen to optimally image the heavier and slower fragments. The ions are detected on an 80-mm MCP with delay line anode and events are stored for off-line analysis as in the LBNL apparatus. The Heidelberg apparatus was calibrated using the 0-eV DEA resonance in SF₆ for electron impact energy correction and to measure the resolution of the electron beam, which was determined to be 280 meV (FWHM). Additionally, the 6.5-eV resonance for O⁻ formation in molecular oxygen [16,21,33] has been used to calibrate the ion momenta.

IV. RESULTS

A. 5.5-eV resonance

H⁻ and NH₂⁻ are both produced from the lower 5.5-eV resonance in the approximate ratio 6:4. In our cold-target recoil-ion momentum spectroscopy experiments, ion kinetic energy was directly measured. The total kinetic-energy release (KER) can be derived from the ion kinetic energy in the case of two-body breakup using momentum and energy conservation through the relation

$$\text{KER} = \frac{M_{\text{target}}}{M_{\text{neutral fragment}}} (\text{KE}_{\text{ion}}). \quad (10)$$

At a nominal electron energy of 5 eV, the H⁻ ion energies are on the order of 1–1.5 eV, while the NH₂⁻ ion energies are only \sim 0.1 eV. In the LBNL experiments, both H⁻ and NH₂⁻ were measured using an effusive source of target gas

molecules. In the Heidelberg experiment, only NH₂⁻ was measured, but with better momentum resolution than in the LBNL experiment since a colder, better collimated beam was produced using a supersonic jet.

Turning first to H⁻, we see from the measured momentum distribution in Fig. 3(a) that ions are scattered mostly perpendicular to the direction of the incident electron beam (which is bottom to top in the figure). The ion kinetic-energy distribution shown in Fig. 3(b) peaks at 1.5 eV with a spread of \sim 2 eV. We note that these values are higher than the 1.0–1.25-eV values reported by Ram and Krishnakumar [15] from their velocity-slice imaging study and the 1.2–1.5-eV values reported by Tronc *et al.* [9]. We have shown that the velocity-slicing method can significantly underestimate the ion kinetic energy [21], which might explain the observed discrepancy with the former data. The smaller discrepancies we find with the data from Tronc *et al.* could be related to the different target temperatures (50 K in their case, comparable to the setup in Heidelberg) affecting the partitioning between KER and internal energy of NH₂.

Figure 3(c) shows the squared modulus of the entrance amplitude (entrance probability) we obtained from the analysis of our fixed-nuclei scattering calculations at the target equilibrium geometry. The result is similar to what was found for the ²A₁ resonance in water [22], with two lobes aligned in the direction of the nitrogen lone pair along the C₃ axis. The larger lobe points away from the NH bonds, indicating that attachment occurs preferentially when the electron is incident from the hydrogen side of the molecule along the C₃ axis. Figure 3(d) compares the calculated and measured ion angular distributions. There is reasonably good agreement between the LBNL measurements and those of Ram and Krishnakumar. The axial recoil prediction, on the other hand, differs from experiment, showing a maximum some 30° larger than what is observed. This is to be expected, since our structure calculations show that there is a significant energy barrier to direct dissociation. When axial recoil breaks down, we can still use the computed entrance amplitudes to predict angular distributions when we have theoretical evidence that points to how the recoil axis rotates following electron attachment, as we have shown in several previous studies [2,4,6]. Our structure calculations show that by holding H-N-H fixed and rotating the third N-H in the direction away from H-N-H, the energy at the top of the barrier drops, becoming equal to the initial resonance energy at \sim 25° rotation. Therefore, to simulate the post attachment flattening needed to overcome the barrier to dissociation, we rotated the entrance probability by 25° in the direction of wider angles before computing the angular distributions. These results are also shown in Fig. 3 and are seen to give much better agreement with experiment.

Turning next to NH₂⁻, the results from the LBNL and Heidelberg experiments are shown in Fig. 4. The measured ion momentum distributions again show that ions are preferentially scattered perpendicular to the direction of the incident electron beam. The Heidelberg measurements also show that as the electron energy is swept across the resonance, the angular distribution remains constant to \sim 5.5 eV, then shifts to larger scattering angles as the electron energy is further increased. This points to a dependence of the trajectory on

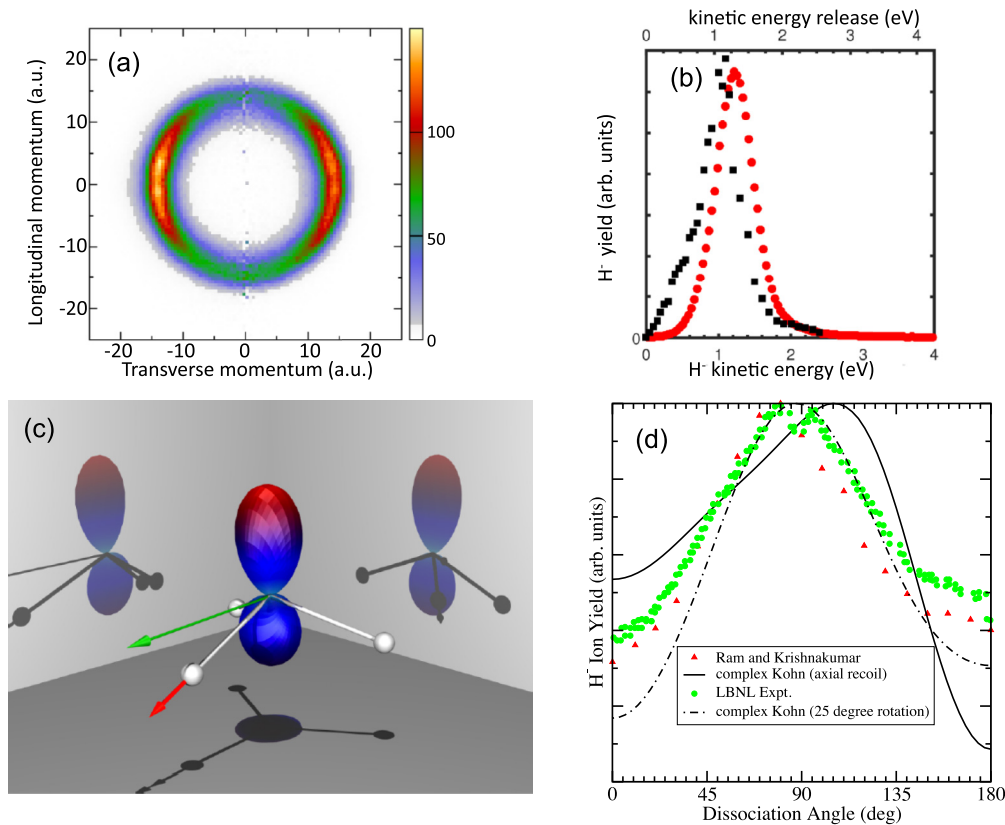


FIG. 3. H^-/NH_3 . (a) LBNL-measured momentum distribution at 5.5 eV electron energy. (b) Ion kinetic-energy release at 5.5 eV, measured at LBNL (red circles) and the data of Ref. [15] (black squares). (c) Entrance probability, with rod balls showing NH bonds, a red arrow showing recoil axis (axial recoil), and a green arrow showing rotated recoil axis (see text). (d) Angular distributions.

the dissociative potential-energy surface on the energy of the initial resonance state. The ion kinetic-energy distribution from the LBNL experiment peaks near 0.1 eV, while the Heidelberg data [cf. Fig. 4(b)] peaks at 0.06 eV, again reflecting the lower supersonic target temperatures (~ 10 K) in the Heidelberg experiment than in the LBNL experiment in which they were closer to room temperature.

The measured and calculated angular distributions are shown in Fig. 5. As explained above, theory predicts that NH_2^- production is a two-step process involving attachment to the 5.5-eV ($\text{H}^- + \text{NH}_2$) resonance followed by charge exchange to the “virtual state” channel at large internuclear separation. Since $\theta_{\text{NH}_2^-} = 180^\circ - \theta_{\text{H}^-}$, theory therefore predicts that the NH_2^- angular distribution should just be the H^- distribution reflected through 90° . This prediction is seen to agree well with the Heidelberg measurements after rotating the entrance probability, as discussed above, and reflecting the H^- distribution through 90° . Best agreement was achieved by averaging the recoil axis about a 20° cone to simulate the finite acceptance angle in the experiment. We note that the agreement between the LBNL measurements and both theory and the Heidelberg measurements is only fair: This is very likely due to the limited momentum resolution for this heavy fragment in the LBNL experiments due to its small kinetic energy. In this case the anion fragment momentum image includes systematic broadening due to the finite volume in

the overlap of the NH_3 target with the low-energy electron beam, resulting in a systematic broadening of the fragment angular distribution. The corresponding volume in the cold jet target of the Heidelberg experiment is significantly smaller and the momentum resolution is therefore much improved. Nevertheless, we find the mutual agreement between the two experiments and the theory is excellent when we use the reflected H^- LBNL measurements for the comparison.

To test our hypothesis of a charge-exchange mechanism producing NH_2^- , we carried out a simplified two-state, time-dependent calculation in a single ($\text{H}-\text{NH}_2$) coordinate. We fit the ground-state energy of neutral ammonia to a Morse potential and computed the ground vibrational state using the $\text{NH}_2\text{-H}$ reduced mass. We used our calculated asymptotic curves (Fig. 2) for the resonance and virtual states, both extrapolated to equilibrium geometry. A wave packet (initial vibrational wave function multiplied by $\sqrt{\Gamma}$ [34–36]) was placed on the resonance curve at R_e and propagated using the calculated Euclidean norm of the full nonadiabatic (derivative) coupling matrix, $\|h\|$ [37–39], to connect the resonance and virtual states. The results shown in Fig. 6 indicate that $\sim 40\%$ of the population is transferred to the lower state, in good agreement with experiment. We also repeated the calculation with a reduced coupling ($\|h\|/10$) and found that $\sim 15\%$ of the initial resonance population was still transferred to the virtual-state channel.

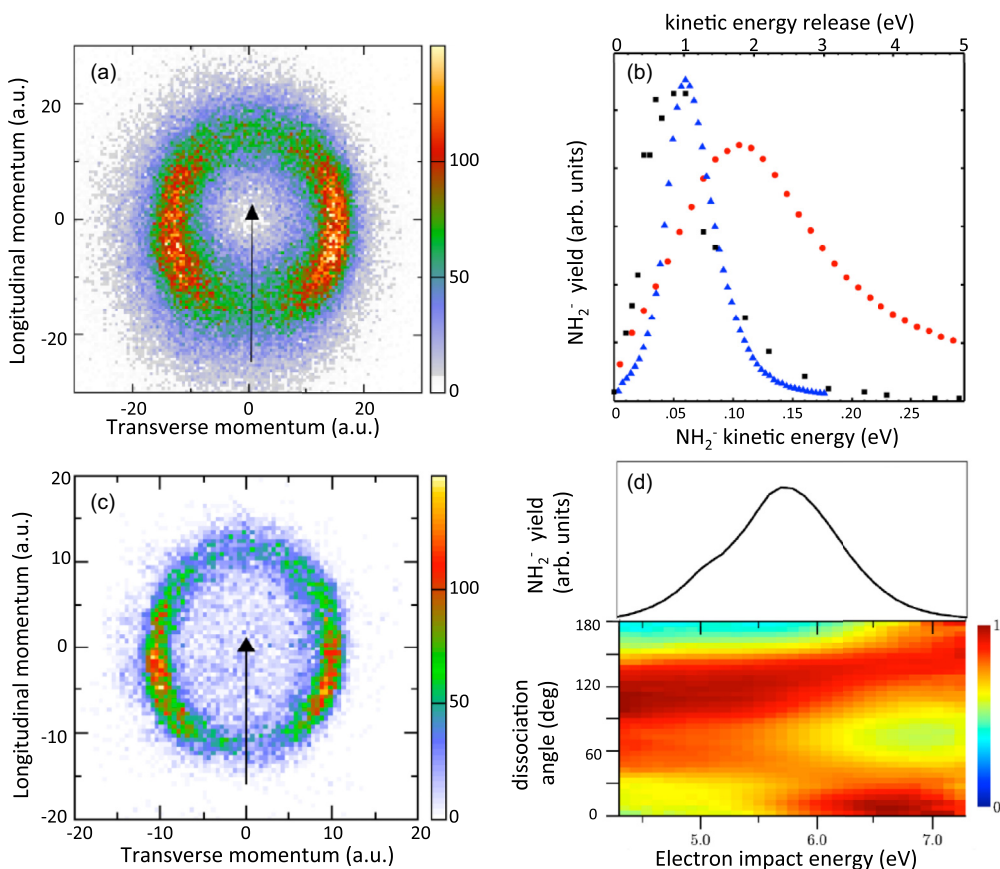


FIG. 4. $\text{NH}_2^-/\text{NH}_3$. (a) LBNL-measured momentum distribution at 5.5 eV; (b) Ion kinetic-energy release at 5 eV, measured at LBNL (red circles), in Heidelberg (blue triangles), and by Ram and Krishnakumar [15] (black squares). (c) Heidelberg-measured momentum distribution at 4.9 eV electron energy. (d) Heidelberg-measured ion yield (top) and angular distributions (bottom) vs electron impact energy.

B. 10.5-eV resonance

H^- is the predominant ion formed from the 10.5-eV resonance, with $\sim 85.5\%$ of the total ion yield going into the $\text{H}^- + \text{NH}_2$ dissociative channel. The measured H^- momentum spectrum at 10 eV nominal electron beam energy is displayed in Fig. 7(a). The distribution shows a strong peak in the backward direction with respect to the incident electron beam.

The corresponding H^- kinetic-energy distribution displayed in Fig. 7(b) is seen to be symmetrically peaked about 4.3 eV with a width of ~ 1.5 eV. The peak KER ($17/16=1.0625$ times H^- kinetic energy) is thus 4.6 eV, which points to $\text{H}^- + \text{NH}_2^*$ (2A_1), whose thermodynamic threshold is 4.77 eV, as the final product channel, as confirmed by the electronic structure calculations we reported above. If NH_2 were being produced in its 2B_1 ground state, we would expect a peak

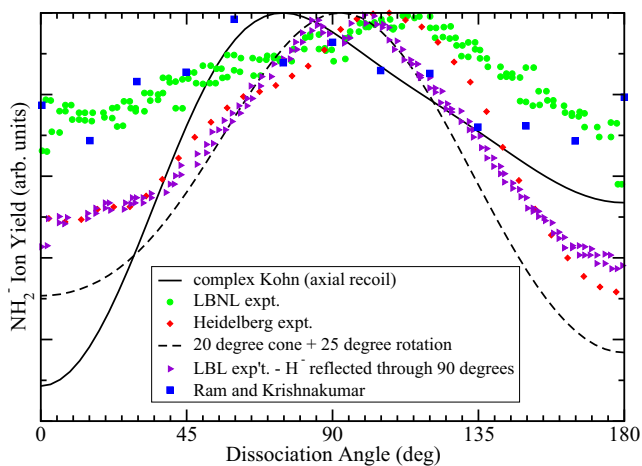


FIG. 5. Angular distributions for $\text{NH}_2^-/\text{NH}_3$ from the 5.5-eV resonance.

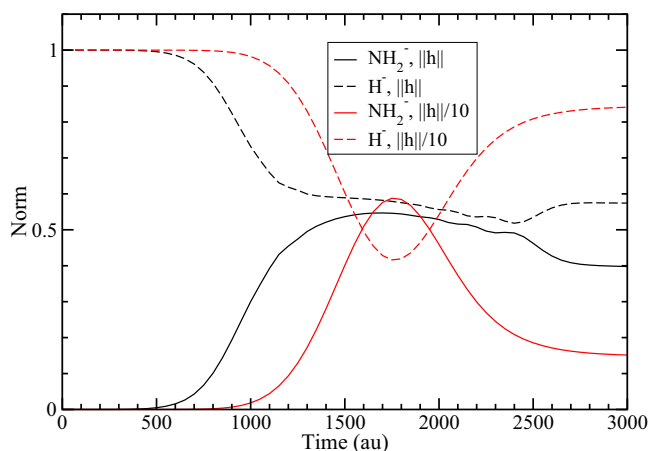


FIG. 6. 1D charge-exchange model.

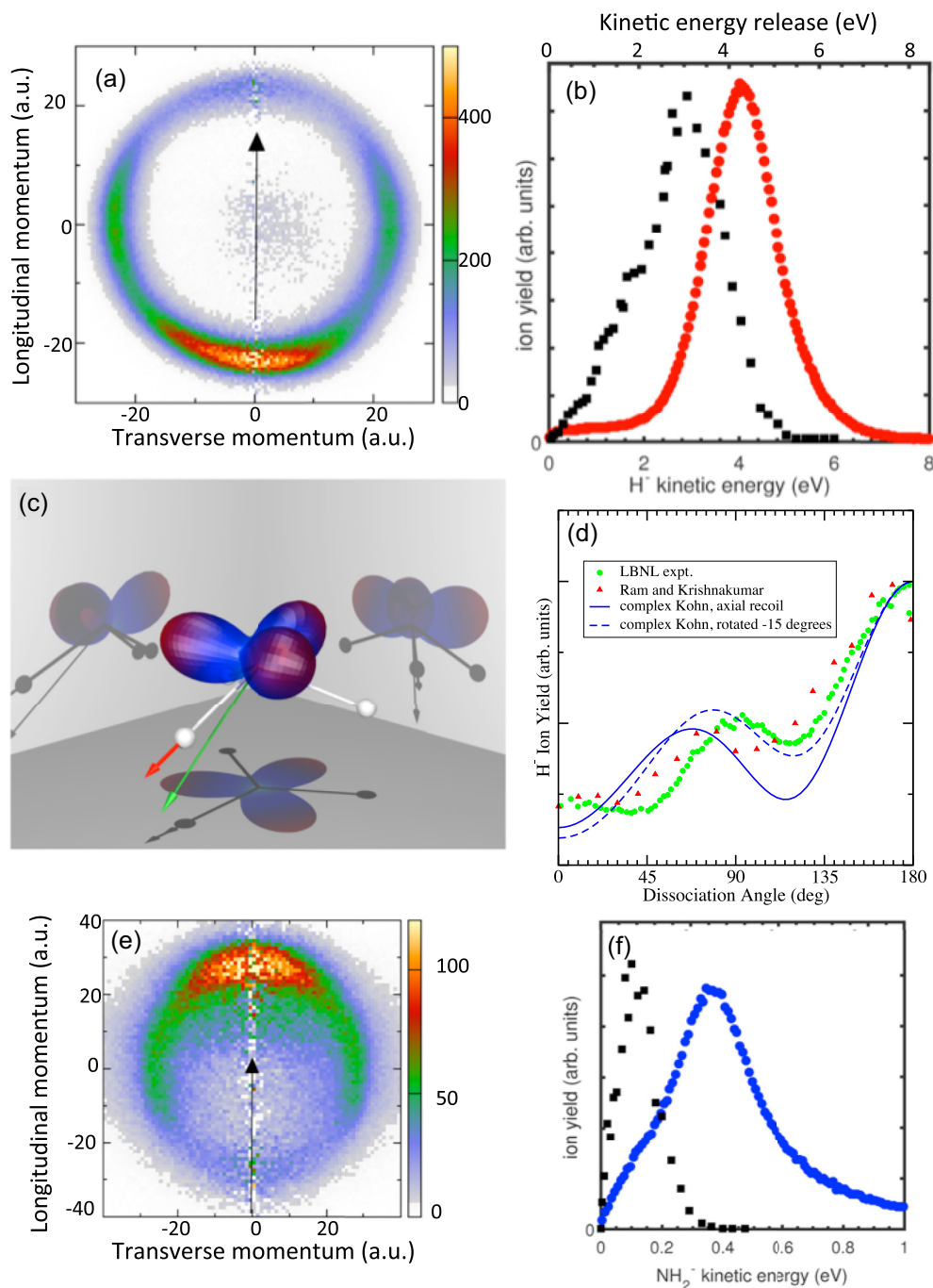


FIG. 7. (a) LBL-measured momentum distribution of $H^- + NH_2^*/NH_3$ at 10 eV electron energy; incident electron direction is from bottom to top. (b) $H^- + NH_2^*/NH_3$ anion kinetic energy and derived total kinetic-energy release for 10 eV electron impact from present experiments at LBNL (red circles); also shown are the 10.5 eV data of Ref. [15] (black squares). (c) Entrance probability, with rod balls showing NH bonds, red arrow showing recoil axis (axial recoil) and green arrow showing rotated recoil axis (see text). (d) H^- angular distributions. (e) NH_2^- angular distribution at 10 eV electron energy. (f) $NH_2^- + H/NH_3$ anion kinetic energy and derived total kinetic-energy release for 10 eV electron impact from present experiments at LBNL (blue circles); also shown are the 10.5 eV data of Ref. [15] (black squares).

H^- kinetic energy of ~ 5.8 eV, which is higher than what we find. Ram and Krishnakumar [15] have reached a similar conclusion, although the ion kinetic-energy distribution they reported peaks close to 3 eV, which, if correct, would mean that the NH_2^* (2A_1) neutral product was being produced with more than 1.6 eV internal energy. Our measurements imply a relatively cold NH_2^* product.

Figure 7(c) shows the *ab initio* entrance probability we derive from an analysis of the 2E resonance S matrix at equilibrium geometry. The resonance is doubly degenerate in C_{3v} symmetry, so the entrance probabilities for the two components were added to produce the displayed result. The resulting probability shows C_{3v} symmetry with lobes pointing away from the three N-H bonds, again indicating that

attachment occurs preferentially when the electron is incident from the hydrogen side of the molecule.

The calculated and measured H^- angular distributions are compared in Fig. 7(d). The present measurements are in reasonably good agreement with those of Ram and Krishnakumar. The theoretical axial recoil result, obtained by averaging the entrance probability about an N-H bond, is in fair agreement with experiment, but better agreement is obtained by rotating the entrance probability by 15° in the direction of smaller N-H angles. This 15° rotation is consistent with the local energy minimum we calculated for the upper resonance [Fig. 1(b)] under umbrella motion.

For the same electron energy of 10 eV we also observe a small yield ($\sim 5\%$ compared to the yield of H^-) of NH_2^- with a momentum distribution and ion kinetic-energy distribution plotted in Figs. 7(e) and 7(f), respectively. The NH_2^- momentum image appears to be a mirror image of the H^- image, strongly suggesting that the two channels are produced from the same 10.5-eV resonance and therefore the same electron attachment entrance probability. A key difference between the two channels, however, is the larger kinetic-energy release, peaked at about 5.8 eV, for the NH_2^- channel, which is consistent with the final states being the same $+H$ asymptote reached from the 5.5-eV resonance. We can only speculate about a mechanism for the small ($< 15\%$) fraction of product ions produced in the $NH_2^- + H$ channel from the 10.5-eV resonance. Our structure calculations do not serve to identify any negative-ion state that could connect the upper resonance state to either the lower ${}^2A'$ resonance surface or the virtual state. One possibility is that the broad 10-eV σ^* shape resonance observed in elastic scattering could provide a coupling between the upper and lower resonances, the latter then populating the $NH_2^- + H$ channel through the charge-exchange mechanism discussed above.

V. SUMMARY AND CONCLUSIONS

In summary, we have combined *ab initio* scattering and electronic structure calculations with momentum-imaging experiments to elucidate the mechanisms and principal dissociation pathways for dissociative electron attachment to ammonia. We have shown that the lower, 5.5-eV, resonance is a doubly excited (Feshbach) state with configuration $3a_14a_1^2$

that feeds both the $H^- + NH_2$ and the $H + NH_2^-$ channels. H^- is produced by a direct process, while NH_2^- production is a two-step process that involves nonadiabatic charge transfer from the resonance state to a lower virtual state at large distances. The fact that the electron affinities of NH_2 and H are almost equal lends the process the character of a symmetric charge-exchange collision. The angular distributions for H^- and NH_2^- are seen to be mirror images of each other, which is consistent with one being established at shorter distances, followed by population of the other channel without much change in the angular distribution. There is a breakdown of axial recoil because of an energy barrier that precludes direct N-H bond scission. Dissociation is accompanied by a flattening (umbrella) motion, an effect we find can be reasonably well described by rotating the entrance probability before computing the angular distributions.

The upper 10.5-eV resonance is found to be a doubly excited 2E state with the configuration $1e^34a_1^2$ which splits into ${}^2A'$ and ${}^2A''$ components when C_{3v} symmetry is broken. The ${}^2A'$ component is found to be dissociative, correlating with $H^- + NH_2^*$ (2A_1). Axial recoil breakdown is found to be less severe in this case, as there is no barrier to direct dissociation. However, we find that a small closing of the HNH angles accompanies dissociation and that the effect can again be well accounted for by a suitable rotation of the entrance probability. The mechanism responsible for the relatively small amount of NH_2^- that is produced from the upper resonance remains something of a mystery. We find no dissociative anion state that connects the upper resonance to the lower channels. We suggest that the broad 10-eV shape resonance seen in elastic electron-ammonia scattering may provide the coupling, but this suggestion is, at this point, purely speculative.

ACKNOWLEDGMENTS

This work was performed under the auspices of the US DOE by LBNL under Contract No. DE-AC02-05CH11231 and was supported by the U.S. DOE, Office of Science, Basic Energy Sciences, Chemical Sciences, Geosciences, and Biosciences Division. This work was also supported in part by the U.S. DOE, Office of Science, Office of Workforce Development for Teachers and Scientists (WDTS) under the Visiting Faculty Program (VFP).

-
- [1] D. J. Haxton, H. Adaniya, D. S. Slaughter, B. Rudek, T. Osipov, T. Weber, T. N. Rescigno, C. W. McCurdy, and A. Belkacem, *Phys. Rev. A* **84**, 030701 (2011).
- [2] D. S. Slaughter, D. J. Haxton, H. Adaniya, T. Weber, T. N. Rescigno, C. W. McCurdy, and A. Belkacem, *Phys. Rev. A* **87**, 052711 (2013).
- [3] A. Moradmand, D. S. Slaughter, D. J. Haxton, T. N. Rescigno, C. W. McCurdy, T. Weber, S. Matsika, A. L. Landers, A. Belkacem, and M. Fogle, *Phys. Rev. A* **88**, 032703 (2013).
- [4] N. Douguet, D. S. Slaughter, H. Adaniya, A. Belkacem, A. E. Orel, and T. N. Rescigno, *Phys. Chem. Chem. Phys.* **17**, 25621 (2015).
- [5] D. J. Haxton, C. W. McCurdy, and T. N. Rescigno, *Phys. Rev. A* **73**, 062724 (2006).
- [6] M. Fogle, D. J. Haxton, A. L. Landers, A. E. Orel, and T. N. Rescigno, *Phys. Rev. A* **90**, 042712 (2014).
- [7] T. E. Sharp and J. T. Dowell, *J. Chem. Phys.* **50**, 3024 (1969).
- [8] R. N. Compton, J. A. Stockdale, and P. W. Reinhardt, *Phys. Rev.* **180**, 111 (1969).
- [9] M. Tronc, R. Azria, and M. B. Arfa, *J. Phys. B* **21**, 2497 (1988).
- [10] P. Rawat, V. S. Prabhudesai, M. Rahman, N. B. Ram, and E. Krishnakumar, *Int. J. Mass Spectrom.* **277**, 96 (2008).
- [11] C. T. Wickham-Jones, K. M. Ervin, G. B. Ellison, and W. C. Lineberger, *J. Chem. Phys.* **91**, 2762 (1989).
- [12] K. L. Stricklett and P. D. Burrow, *J. Phys. B* **19**, 4241 (1986).

- [13] A. D. Walsh and P. A. Warsop, *Trans. Faraday Soc.* **57**, 345 (1961).
- [14] M. Furlan, M-J. Hubin-Franskin, J. Delwiche, D. Roy, and J. E. Collin, *J. Chem. Phys.* **82**, 1797 (1985).
- [15] N. B. Ram and E. Krishnakumar, *J. Chem. Phys.* **136**, 164308 (2012).
- [16] D. Nandi, V. S. Prabhudesai, E. Krishnakumar, and A. Chatterjee, *Rev. Sci. Instrum.* **76**, 053107 (2005).
- [17] A. Jain and D. G. Thompson, *J. Phys. B* **16**, 2593 (1983).
- [18] H. P. Pritchard, M. A. P. Lima, and V. McKoy, *Phys. Rev. A* **39**, 2392 (1989).
- [19] T. N. Rescigno, B. H. Lengsfeld, C. W. McCurdy, and S. D. Parker, *Phys. Rev. A* **45**, 7800 (1992).
- [20] J. Ullrich, R. Moshhammer, A. Dorn, R. Dörner, L. P. H. Schmidt, and H. Schmidt-Böcking, *Rep. Prog. Phys.* **66**, 1463 (2003).
- [21] H. Adaniya, D. S. Slaughter, T. Osipov, T. Weber, and A. Belkacem, *Rev. Sci. Instrum.* **83**, 023106 (2012).
- [22] H. Adaniya, B. Rudek, T. Osipov, D. J. Haxton, T. Weber, T. N. Rescigno, C. W. McCurdy, and A. Belkacem, *Phys. Rev. Lett.* **103**, 233201 (2009).
- [23] T. N. Rescigno, B. H. L. III, and C. W. McCurdy, in *Modern Electronic Structure Theory*, edited by D. R. Yarkony (World Scientific, Singapore, 1995), Vol. 1, p. 501.
- [24] W. J. Hunt and W. A. Goddard III, *Chem. Phys. Lett.* **3**, 414 (1969).
- [25] T. H. Dunning, *J. Chem. Phys.* **53**, 2823 (1970).
- [26] S. R. Langford, A. J. Orr-Ewing, R. A. Morgan, C. M. Western, M. N. R. Ashfold, A. Rijkenberg, C. R. Scheper, W. J. Buma, and C. A. de Lange, *J. Chem. Phys.* **108**, 6667 (1998).
- [27] J. Macek, *Phys. Rev. A* **2**, 1101 (1970).
- [28] J. R. Taylor, *Scattering Theory: The Quantum Theory of Nonrelativistic Collisions* (Wiley & Sons, New York, 1972) p. 246.
- [29] H. Lischka, R. Shepard, I. Shavitt, R. M. Pitzer, M. Dallos, Th. Müller, P. G. Szalay, F. B. Brown, R. Ahlrichs, H. J. Böhm *et al.*, Columbus, an ab initio electronic structure program release 7.0 (2012).
- [30] R. A. Kendall, T. H. Dunning, and R. J. Harrison, *J. Chem. Phys.* **96**, 6796 (1992).
- [31] R. G. Newton, *Scattering Theory of Waves and Particles* (Springer-Verlag, 1982) p. 357 .
- [32] C. Schröter, A. Rudenko, A. Dorn, R. Moshhammer, and J. Ullrich, *Nucl. Instrum. Methods Phys. Res., Sect. A* **536**, 312 (2005).
- [33] A. Moradmand, J. Williams, A. L. Landers, and M. Fogle, *Rev. Sci. Instrum.* **84**, 033104 (2013).
- [34] T. F. O'Malley, *Phys. Rev.* **150**, 14 (1966).
- [35] L. Dube and A. Herzenberg, *Phys. Rev. A* **20**, 194 (1979).
- [36] A. U. Hazi, T. N. Rescigno, and M. Kurilla, *Phys. Rev. A* **23**, 1089 (1981).
- [37] B. H. Lengsfeld and D. R. Yarkony, *J. Chem. Phys.* **84**, 348 (1986).
- [38] D. R. Yarkony, *Rev. Mod. Phys.* **68**, 985 (1996).
- [39] H. Lischka, M. Dallos, P. G. Szalay, D. R. Yarkony, and R. Shepard, *J. Chem. Phys.* **120**, 7322 (2004).